UC Santa Cruz
UC Santa Cruz Previously Published Works

Title
Effect of CZT System Characteristics on Compton Scatter Event Recovery

Permalink
https://escholarship.org/uc/item/5f5695n1

Journal
IEEE Transactions on Radiation and Plasma Medical Sciences, 4(1)

ISSN
2469-7311

Authors
Yang, Sheng
Li, Mohan
Reed, Michael
et al.

Publication Date
2020

DOI
10.1109/trpms.2019.2915054

Peer reviewed

Effect of CZT system characteristics on Compton scatter event recovery

Sheng Yang [Student Member, IEEE],

Department of Nuclear, Plasma, and Radiological Engineering, University of Illinois at Urbana-Champaign, Urbana, IL, 61801 USA.

Mohan Li [Student Member, IEEE],

Department of Nuclear, Plasma, and Radiological Engineering, University of Illinois at Urbana-Champaign, Urbana, IL, 61801 USA.

Michael Reed,

Kromek USA/eV Products, Saxonburg, PA, 16056, USA.

James Hugg,

Kromek USA/eV Products, Saxonburg, PA, 16056, USA.

Henry Chen,

Kromek USA/eV Products, Saxonburg, PA, 16056, USA.

Shiva Abbaszadeh [Member, IEEE]

Department of Nuclear, Plasma, and Radiological Engineering, University of Illinois at Urbana-Champaign, Urbana, IL, 61801 USA.

Abstract

Improving 511 keV photon detection sensitivity is a common goal for positron emission tomography system designers. One attractive approach to increase sensitivity is recovering events that are normally rejected. The kinematics of Compton scattering can be used to recover the line of response through direction difference angle (DDA). The uncertainty of DDA is determined by the energy and spatial resolution of a system. In this work, we evaluated the performance of small animal CZT-based positron emission tomography systems with energy resolution of 1%, 4%, and 6% and different spatial resolution based on prior work for guiding new design efforts. Designs with energy resolution limited by counting statistics and by electronic noise were considered. The influence of modifying the conventional energy window and uncertainty of DDA was investigated. For a system with 4% energy resolution and limited by electronic noise, the figure of merit of noise equivalent count increases by 65% as the lower energy bound increases from 471 keV to 493 keV. If the system-wide energy resolution becomes worse than 4% of the full width half maximum at 511 keV, going to a pixel size finer than 1 mm has very limited effect in reducing total angular uncertainty. For a system with 1% energy resolution, as the spatial resolution improves from 1 mm to 0.5 mm, the contrast-to-noise ratio increases by 9%.

Keywords

Compton Recovery; CZT; PET; Sensitivity

I. Introduction

CADMIUM telluride (CdTe) and cadmium zinc telluride (CZT) are highly developed semiconductors for direct detection of X-ray and gamma rays [1]. They are commercially available in detectors for mammography, single-photon emission computerized tomography (SPECT) and homeland security. Several laboratories have investigated the spatial, energy, and timing resolution of CdTe and CZT (with different dimensions and electrode designs) as a detector technology for detecting 511 keV annihilation photons in positron emission tomography (PET) scanners [2]–[5]. Energy resolution of 1% full width at half maximum (FWHM) at 662 keV and timing resolution of 10 ns FWHM have been demonstrated using CZT [6]. The majority of preclinical and clinical PET systems make use of indirect conversion of 511 keV photons through scintillator crystals attached to a photomultiplier tube, avalanche photodiode, or silicon photomultiplier (SiPM) for detection [7]–[9]. Compared to scintillators, the cost, uniformity, limited coincidence time resolution, and low photoelectric probability for 511 keV photons were the main drawbacks of CZT for the PET application. However, progress in process development [10], novel detector designs [11], [12], measurement methods [13], and implementation of algorithms [14]–[16] have addressed these challenges over the past decade.

Traveling Heater Method (THM) accelerated significant improvement and breakthrough in large volume CZT crystal growth technology, both performance and yield, leading to a significant cost reduction of CZT detectors compared to previous high performance CZT produced by the low yield High-Pressure Bridgman method. Large uniform CZT crystal block ($4{\times}4{\times}0.5$ cm^3) with an edge-on orientation can be stacked on top of each other to build a preclinical system. 4 cm thick CZT can provide 86% intrinsic efficiency for 511 keV singles. In addition, because of the high Compton scatter fraction (table I [17]), at 511 keV, there is an opportunity to improve the sensitivity by considering multiple interaction photon events (MIPEs). Recovering the first interaction in MIPEs using Compton kinematics relies on both recorded energy and position to determine the sequence of interactions and create the line of response (LOR). This technique will have substantial impact on sensitivity and contrast recovery of the system. CZT is an excellent candidate for highly accurate recovery of MIPEs due to its high-energy resolution (2% for CZT vs >10% for LSO) and accurate depth of interaction.

In Compton recovery for the PET application, the direction difference angle (DDA), $\theta_{DDA} = |\theta_E - \theta_P|$, can be used to select the sequence of interactions, where θ_E is the Compton scattering angle, and θ_p is the angle based on event positions [18]–[20]. The Compton scattering angle θ_E is determined by

$$\theta_E = \cos^{-1}\left(1 - mc^2\left(\frac{1}{E_s} - \frac{1}{E_i}\right)\right), \tag{1}$$

where mc^2 is the rest mass energy of an electron, E_i is the incident photon energy and E_s is the scattered photon energy. The θ_p is determined as the angle between the incident and scattered photon

$$\theta_p = \cos^{-1}\left(\frac{\mathbf{A} \cdot \mathbf{B}}{|\mathbf{A} \cdot \mathbf{B}|}\right), \qquad (2)$$

where $\mathbf{A}$ and $\mathbf{B}$ are the vectors of the incident and scattered photons, respectively, calculated by the position information of detected events. Yoon *et al.* [19] investigated the angular uncertainty due to effects of Doppler broadening, pixelization effect, and energy broadening with a CZT-based PET system. The energy resolution and spatial resolution of the system was 1% and $1 \times 0.5 \times 2.5$ mm^3 respectively. Doppler broadening had a minimal impact on the angular uncertainty compared to that of spatial and energy resolution. Although, from their results, the spatial resolution contributed more to the angular uncertainty, the effect of spatial resolution and energy resolution in the system performance such as sensitivity and contrast-to-noise ratio (CNR) remained to be investigated.

In this work, we determined the angular uncertainty in Compton scatter recovery and the system level performance for various spatial and energy resolution conditions of a small animal CZT-based PET system. The detectors with different characteristics were simulated and angular uncertainties in space and energy were calculated accordingly. The influence of energy window selection on the sensitivity of detectors was also investigated. The results of this work will guide design decisions on the targeted energy and spatial resolution.

II. Methods and materials

A. Simulation setup

In order to investigate the effect of spatial and energy resolution of the CZT detectors on imaging performance, a four-panel system with a field of view (FOV) of $40 \times 40 \times 40$ mm^3 was considered. Each panel included 8 tightly packed $40 \times 40 \times 5$ mm^3 CZT crystals. The simulation time was 28 secs.

A customized phantom was used in this study (figure 1) consisting of a tissue equivalent plastic, PMMA, cylinder with a 22 mm height and a 22 mm diameter. The cylinder was filled with a ^{18}F water phantom with 20 mm height and 20 mm diameter as a background region. 3 cylindrical compartments inside the water phantom were filled with an aqueous solution of ^{18}F whose concentration was 8 times the background. The total activity was 286 μCi. The diameter of compartments were 1, 2, and 3 mm respectively and 5 mm from the center.

The hit mode file of GATE [21] was processed to generate the LORs from the interactions recorded in the CZT crystals. The LORs were processed with a listmode OS-EM algorithm [22] to reconstruct images. A time window of 20 ns based on previously published results was used [5], [23].

After performing the simulation, six scenarios using different energy resolution (1%, 4%, and 6% FWHM at 511 keV) and spatial resolution ($0.5 \times 0.5 \times 0.5$ mm^3, $1 \times 1 \times 1$ mm^3, $1 \times 3 \times 0.5$ mm^3, $1 \times 3 \times 1$ mm^3, and $1 \times 5 \times 1$ mm^3) were considered based on previous published studies [11], [19], [24]–[26]. Table II summarizes the scenarios considered in post-processing for each system. Based on different spatial resolution, the CZT crystal was segmented into

voxels, and the position of an interaction was moved to the center of the voxel where the interaction happened.

Two methods were considered to blur the deposited energy, electronics limited method [27] and statistic limited method [28]. For the electronics limited method, all the deposited energy had the same FWHM as the FWHM at 511 keV. For the statistic limited method, the energy resolution of the deposited energy (E) was calculated by Eq. (3)

$$R_E = R_{511keV} \cdot \sqrt{\frac{511}{E}}, \tag{3}$$

where R_E and R_{511keV} are the energy resolution of the deposited energy and 511 keV respectively. Then, the FWHM of the deposited energy was determined.

The system with a 4% energy resolution was used to investigate the influence of energy window on a figure of merit, modified noise equivalent count (NECm). NECm is determined by

$$NECm = \frac{T^2}{T + R + C + S}, \tag{4}$$

where T is the number of correctly positioned true coincidences, R is the number of random coincidences, C is the number of mispositioned true coincidences, and S is the number of scattered coincidences [20].

The energy threshold of a system defines the minimal deposited energy that can be detected. A 511 keV photon deposits less than 100 keV when the scattering angle is smaller than $40°$. Therefore, a system with a 100 keV energy threshold is not able to detect scattered photons with the scattering angle lower than $40°$. In this study, an energy threshold of 50 keV was used. That is, the events with the deposited energy below the energy threshold were filtered from the simulation data. With a 50 keV energy threshold, 6% true Compton-photoelectric coincidence were discarded but no true photoelectric-photoelectric coincidence was discarded. The results were from a system with a 4% energy resolution at 511 keV and a 493-551 keV energy window. The detected events were blurred with the electronic limited blurring method.

A custom code was developed to generate coincidences. Two types of coincidences were considered in this study: 1) coincidence generated by two photoelectric events and 2) one photoelectric event and one Compton event followed by a photoelectric event. After the energy blurring, all the hits within the time window were considered as a possible coincidence. If the total energy of the hits in either panel was not within the given energy window, the coincidence was rejected. The interaction type of each coincidence was determined by the number of the hits in each panel. If each panel only has one hit, the coincidence was labeled as a photoelectric-photoelectric (PP) coincidence. If one panel has one hit and the other panel has two hits, the coincidence was labeled as a photoelectric-Compton (PC) coincidence. The PC coincidences were further processed to determine correct sequences and generate LORs. If there were two or more hits in both panels, the

coincidence was labeled as a Compton-Compton coincidence but not used in the Compton recovery. There are two θ_{DDA} computed due to the different possible interaction sequences of Compton events. The sequence with a smaller θ_{DDA} is considered as the correct sequence. After the correct sequence is determined, the LOR is generated based on the position of the photoelectric event and the first interaction position of the Compton event. More details can be found in [18]–[20]. The sensitivity of a system was defined as the ratio (or percentage) of the number of events assigned to system LORs (used to reconstruct images) to the total number of disintegrations.

B. Angular uncertainty

To quantify the uncertainty in a θ_{DDA}, the uncertainty due to energy broadening and pixelization effect was calculated and, then, the uncertainty of θ_{DDA} was obtained. Note that we did not consider Doppler broadening when determining the angular uncertainty. The uncertainty of θ_E was derived from Eq. (1) after the energy blurring. Similarly, the uncertainty of θ_P was calculated by Eq. (2) after binning the interaction position. A reconstructed θ_{DDA} can be calculated from the difference of blurred θ_E and binned θ_P. The uncertainty of θ_{DDA} is the difference between the reconstructed θ_{DDA} and the θ_{DDA} calculated from the real positions of the interaction and the true energy of the photon.

C. Performance evaluation

The effect of energy and spatial resolution on the performance of the system including MIPEs was measured in terms of the CNR and contrast. 3 background regions were selected to determine the mean and standard deviation of CNR and contrast. The voxel size of images was $0.25 \times 0.25 \times 0.25$ mm^3. The CNR and contrast were evaluated using the following equations [20]

$$CNR = \frac{I_{hot} - I_{background}}{\sigma_{background}}, \tag{5}$$

$$Contrast = \frac{I_{hot} - I_{background}}{I_{background}}, \tag{6}$$

where I_{hot} and $I_{background}$ are the mean intensity in hot rod and in the background region of interest (ROI), respectively, and $\sigma_{background}$ is the standard deviation of the intensity of the background ROI.

III. Results

A. Angular uncertainty

Figure 2 shows the uncertainty distribution with the 1% energy resolution and $1 \times 1 \times 1$ mm^3 spatial resolution and 4% energy resolution and $0.5 \times 0.5 \times 0.5$ mm^3 spatial resolution. From figure 2 (a), the dominant effect on the uncertainty is pixelization effect while, in figure 2 (b), the energy broadening effect contributes more to the uncertainty. Therefore, both energy and spatial resolution contribute to the uncertainty in direction difference angle

and their relative contributions are dependent on their absolute value. If the system-wide energy resolution becomes worse than 4% FWHM at 511 keV, going to pixel size finer than 1 mm has limited effect in reducing total angular uncertainty.

Table II shows the average of the absolute uncertainty ($\bar{\sigma}$) of θ_P and θ_E over all the PC coincidence with the energy resolution of 1%, 4%, and 6% FWHM at 511 keV and different spatial resolutions.

B. Influence of energy window

Figure 3 shows the Compton energy spectrum with the electronic noise limited blurring method. The energy resolution was 4% FWHM at 511 keV. Compton events were grouped into two categories, the first category is true Compton event and the second category is mispositioned and scattered Compton events. The first category (in blue) contains events with one Compton scatter followed by a photoelectric interaction, both of which are above the system energy threshold, and the annihilation photon did not scatter in the phantom. The second category (in orange) contains MIPEs whose annihilation photon scattered in the phantom or had one or more additional Compton scatter interactions which were below the energy threshold. The overlapping area from 470 to 511 keV is higher than the area of that from 511 to 552 keV. This suggests that increasing the lower bound of the energy window could help reject the coincidences of the second category. Three energy lower bounds (471, 482, 493 keV) were chosen. They are 2, 1.5, and 1 FWHM apart from 511 keV respectively.

Table III shows the percentage decrease of true, mispositioned, scattered, and random photoelectric-Compton coincidence (PC coincidence) with 482 and 493 keV lower energy bounds compared with the 471 keV lower bound case. Note that the upper bound was fixed at 551 keV for the three cases. The energy blurring method was electronic noise limited. For lower bound of 482 and 493 keV cases, the NECm including PP and PC coincidence increased by 30% and 65% respectively compared with the 471 keV lower bound case.

Figure 4 shows the Compton energy spectrum with the statistic noise limited blurring method. The photon peak of true Compton events is the same as a Gaussian with a 4% FWHM at 511 keV. By comparing figure 3 and 4, the FWHM of the photopeak with the statistic noise limited blurring method is smaller than the FWHM of the peak with the electronics noise limited blurring method. This difference is caused by the different FWHM at the different deposited energy for the statistic limited blurring method. The FWHM with the statistic limited blurring method becomes smaller as the deposited energy decreases while the FWHM with the electronics limited method is the same for all the deposited energy. In addition, the FWHM of the photopeak is the root of the sum of squares of FHWM of each deposited energy. As a result, the FWHM of the photopeak with the statistic limited blurring method is narrower than the photopeak with the electronics limited method.

Table IV shows the percentage decrease of true, mispositioned, scattered, and random PC coincidences with 482 and 493 keV lower energy bounds compared with the 471 keV lower bound case. Note that the upper bound was fixed at 551 keV for the three cases. The energy blurring method was statistic noise limited. The difference in the FWHM with the two different method results in the different percentage decrease as the lower bound increases.

The percentage decrease of true PC coincidence of the electronics limited method is 6% higher than that of the statistic limited method. For lower bound of 482 and 493 keV cases, the NECm including PP and PC coincidence increased by 37% and 103% respectively compared with the 471 keV lower bound case.

C. System performance

Table V shows the percentage of photoelectric-photoelectric coincidences (PP) and photoelectric-Compton coincidences (PC) when no energy threshold was applied versus using 50 keV threshold. This result was calculated with 4% energy resolution at 511 keV, a 493-551 keV energy window, and $1\times3\times0.5$ mm^3 spatial resolution.

Table VI shows the percentage of PC coincidences that were accurately recovered by Compton recovery algorithm. The percentage was calculated as the ratio of the number of corrected recovered true PC coincidences to the number of all PC coincidences. Moving from $1\times1\times1$ mm^3 to $0.5\times0.5\times0.5$ mm^3 spatial resolution at 1% energy resolution does not yield substantial benefit in terms of accurately recovered percentage. A large change is observed when moving to 4% energy resolution and $1\times3\times0.5$ mm^3 spatial resolution.

Table VII shows the sensitivity with and without Compton recovery. The sensitivity increases by a factor of ~3.4 when including the PC coincidences.

To compare the sensitivity of scintillator-based PET systems, the parameters of the system geometry were listed in table VIII. The sensitivity of the systems is from scintillator PET systems, from 4% to 7% [29], [30]. The sensitivity of the CZT system could be improved by including coincidences that undergo Compton scatter in both panels (CC coincidence).

D. Image performance

Three cases (listed in table IX) were selected to evaluate the performance of the system with different energy and spatial resolution. Figures 5, 6, and 7 show reconstructed images using only PP coincidences, PP and PC coincidences recovered using the algorithm described in this work, and PP and PC coincidences recovered using a randomly selected event sequence (i.e., one of the Compton events was chosen randomly to form the LOR). The number of iteration used for image reconstruction was selected to maximize the CNR of the images. Tables IX and X show the CNR and contrast of the three cases. As the spatial resolution and energy resolution improve, the CNR and contrast increase accordingly. For the 1% energy resolution, the CNR of the image with only PP coincidences was improved by 9% as the spatial resolution changed from $1 \times 1 \times 1$ to $0.5 \times 0.5 \times 0.5$ mm^3. For the same energy and spatial resolution, the CNR increased after the PC coincidences were included while the contrast decreased. Table XI shows the percentage increase of CNR of reconstructed images after including PC coincidences. For 1% energy resolution, as the spatial resolution changed from $1 \times 1 \times 1$ to $0.5 \times 0.5 \times 0.5$ mm^3, the CNR increased by 6.5%, 4%, and 7%, respectively, for 3, 2 and 1 mm hot rods. Therefore, improving the spatial resolution at 1% energy resolution can slightly improve the CNR by including PC coincidences. Comparing 1% energy resolution and spatial resolution $0.5 \times 0.5 \times 0.5$ mm^3 case with 4% energy resolution and $1 \times 3 \times 0.5$ mm^3 spatial resolution case, the CNR improved about 50% after including PC coincidences.

IV. Conclusions

In this work, we calculated and compared the angular uncertainty for different energy and spatial resolutions and investigated the influence of energy window on identifying multiple interaction photon events in Compton recovery. Increasing the lower bound of the energy window can reduce the number of the mispositioned and scattered coincidences and, consequently, increases the NECm. In a system limited by electronics noise, it could be beneficial to increase the energy window for identifying Compton scattering events (that deposit all of their energy) compared with the energy window for the photoelectric event. With the improvement of the energy and spatial resolution of a system, the uncertainty of θ_{DDA} decreases and more LORs can be recovered from Compton events. As a result, the percentage increase of CNR after including the PC events increased as the energy resolution and spatial resolution improved. In the future work, Compton-Compton coincidences could be recovered through more complex DDA algorithm to increase the sensitivity of PET systems.

Acknowledgment

References

[1]. Del Sordo S, Abbene L, Caroli E, Mancini AM, Zappettini A, and Ubertini P, "Progress in the development of CdTe and CdZnTe semiconductor radiation detectors for astrophysical and medical applications," Sensors, vol. 9, no. 5, pp. 3491–3526, 2009. [PubMed: 22412323]

[2]. Yin Y, Chen X, Li C, Wu H, Komarov S, Guo Q, Krawczynski H, Meng L-J, and Tai Y-C, "Evaluation of PET imaging resolution using 350μm pixelated CZT as a VP-PET insert detector," IEEE Transactions on Nuclear Science, vol. 61, no. 1, pp. 154–161, 2014.

[3]. Zhang F, He Z, Xu D, and Meng L, "Feasibility study of using two 3-D position sensitive czt detectors for small animal PET," in Nuclear Science Symposium Conference Record, 2005 IEEE, vol. 3 IEEE, 2005, pp. 4–pp.

[4]. Drezet A, Monnet O, Mathy F, Montemont G, and Verger L, "CdZnTe detectors for small field of view positron emission tomographic imaging," Nuclear Instruments and Methods in Physics Research Section A: Accelerators, Spectrometers, Detectors and Associated Equipment, vol. 571, no. 1-2, pp. 465–470, 2007.

[5]. Abbaszadeh S and Levin CS, "New-generation small animal positron emission tomography system for molecular imaging," Journal of Medical Imaging, vol. 4, no. 1, p. 011008, 2017. [PubMed: 28097211]

[6]. Meng LJ and He Z, "Exploring the limiting timing resolution for large volume CZT detectors with waveform analysis," Nuclear Instruments and Methods in Physics Research Section A: Accelerators, Spectrometers, Detectors and Associated Equipment, vol. 550, no. 1, pp. 435–445, 2005.

[7]. Watanabe M, Okada H, Shimizu K, Omura T, Yoshikawa E, Kosugi T, Mori S, and Yamashita T, "A high resolution animal PET scanner using compact PS-PMT detectors," in Nuclear Science Symposium, 1996. Conference Record., 1996 IEEE, vol. 2 IEEE, 1996, pp. 1330–1334.

[8]. Dokhale P, Silverman R, Shah KS, Grazioso R, Farrell R, Glodo J, McClish M, Entine G, Tran V, and Cherry SR, "Performance measurements of a depth-encoding PET detector module based on

position-sensitive avalanche photodiode readout," Physics in Medicine & Biology, vol. 49, no. 18, p. 4293, 2004. [PubMed: 15509066]

[9]. Schaart DR, van Dam HT, Seifert S, Vinke R, Dendooven P, Löhner H, and Beekman FJ, "A novel, SiPM-array-based, monolithic scintillator detector for PET," Physics in Medicine & Biology, vol. 54, no. 11, p. 3501, 2009. [PubMed: 19443953]

[10]. Chen H, Awadalla S, Iniewski K, Lu P, Harris F, Mackenzie J, Hasanen T, Chen W, Redden R, Bindley G et al., "Characterization of large cadmium zinc telluride crystals grown by traveling heater method," Journal of Applied Physics, vol. 103, no. 1, p. 014903, 2008.

[11]. Gu Y, Matteson J, Skelton R, Deal A, Stephan E, Duttweiler F, Gasaway T, and Levin C, "Study of a high-resolution, 3D positioning cadmium zinc telluride detector for PET," Physics in Medicine and Biology, vol. 56, no. 6, p. 1563, 2011. [PubMed: 21335649]

[12]. Meng L-J, Tan J, Spartiotis K, and Schulman T, "Preliminary evaluation of a novel energy-resolved photon-counting gamma ray detector," Nuclear Instruments and Methods in Physics Research Section A: Accelerators, Spectrometers, Detectors and Associated Equipment, vol. 604, no. 3, pp. 548–554, 2009.

[13]. Tao L, Daghighian HM, and Levin CS, "A promising new mechanism of ionizing radiation detection for positron emission tomography: modulation of optical properties," Physics in Medicine & Biology, vol. 61, no. 21, p. 7600, 2016. [PubMed: 27716640]

[14]. Comanor K, Virador P, and Moses W, "Algorithms to identify detector compton scatter in PET modules," IEEE Transactions on Nuclear Science, vol. 43, no. 4, pp. 2213–2218, 1996.

[15]. Pratx G and Levin CS, "Bayesian reconstruction of photon interaction sequences for high-resolution PET detectors," Physics in Medicine and Biology, vol. 54, no. 17, p. 5073, 2009. [PubMed: 19652293]

[16]. Gillam JE, Solevi P, Oliver JF, Casella C, Heller M, Joram C, and Rafecas M, "Sensitivity recovery for the AX-PET prototype using inter-crystal scattering events," Physics in Medicine & Biology, vol. 59, no. 15, p. 4065, 2014. [PubMed: 24988897]

[17]. Abbaszadeh S, Chinn G, and Levin CS, "Effect of energy threshold in positioning true coincidences that undergo detector scatter for a sub-mm resolution CZT-based PET system," in 2015 IEEE Nuclear Science Symposium and Medical Imaging Conference (NSS/MIC). IEEE, 2015, pp. 1–3

[18]. Chinn G and Levin CS, "A maximum NEC criterion for compton collimation to accurately identify true coincidences in PET," IEEE Transactions on Medical Imaging, vol. 30, no. 7, pp. 1341–1352, 2011. [PubMed: 21317079]

[19]. Yoon C, Lee W, and Lee T, "Simulation for CZT compton PET (Maximization of the efficiency for PET using Compton event)," Nuclear Instruments and Methods in Physics Research Section A: Accelerators, Spectrometers, Detectors and Associated Equipment, vol. 652, no. 1, pp. 713–716, 2011.

[20]. Abbaszadeh S, Chinn G, and Levin CS, "Positioning true coincidences that undergo inter-and intra-crystal scatter for a sub-mm resolution cadmium zinc telluride-based pet system," Physics in Medicine & Biology, vol. 63, no. 2, p. 025012, 2018. [PubMed: 29131809]

[21]. Jan S, Santin G, Strul D, Staelens S, Assie K, Autret D, Avner S, Barbier R, Bardies M, Bloomfield P et al., "Gate: a simulation toolkit for PET and SPECT," Physics in Medicine & Biology, vol. 49, no. 19, p. 4543, 2004. [PubMed: 15552416]

[22]. Cui J.-y., Pratx G, Prevrhal S, and Levin CS, "Fully 3D listmode time-of-flight PET image reconstruction on GPUs using CUDA," Medical physics, vol. 38, no. 12, pp. 6775–6786, 2011. [PubMed: 22149859]

[23]. Abbaszadeh S, Gu Y, Reynolds PD, and Levin CS, "Characterization of a sub-assembly of 3D position sensitive cadmium zinc telluride detectors and electronics from a sub-millimeter resolution pet system," Physics in Medicine & Biology, vol. 61, no. 18, p. 6733, 2016. [PubMed: 27551981]

[24]. Levin CS, Foudray AM, and Habte F, "Impact of high energy resolution detectors on the performance of a PET system dedicated to breast cancer imaging," Physica Medica, vol. 21, pp. 28–34, 2006. [PubMed: 17645990]

[25]. Abbaszadeh S, Gu Y, Reynolds PD, and Levin CS, "Characterization of a sub-assembly of 3D position sensitive cadmium zinc telluride detectors and electronics from a sub-millimeter resolution PET system," Physics in Medicine and Biology, vol. 61, no. 18, p. 6733, 2016 [Online]. Available: http://stacks.iop.org/0031-9155/61/i=18/a=6733 [PubMed: 27551981]

[26]. Ishii K, Kikuchi Y, Matsuyama S, Kanai Y, Kotani K, Ito T, Yamazaki H, Funaki Y, Iwata R, Itoh M et al., "First achievement of less than 1 mm FWHM resolution in practical semiconductor animal PET scanner," Nuclear Instruments and Methods in Physics Research Section A: Accelerators, Spectrometers, Detectors and Associated Equipment, vol. 576, no. 2-3, pp. 435–440, 2007.

[27]. Beer AC, Willardson RK, and Weber ER, Semiconductors for room temperature nuclear detector applications. Academic Press, 1995, vol. 43.

[28]. Knoll GF, Radiation detection and measurement. John Wiley & Sons, 2010.

[29]. Visser EP, Disselhorst JA, Brom M, Laverman P, Gotthardt M, Oyen WJ, and Boerman OC, "Spatial resolution and sensitivity of the Inveon small-animal PET scanner," Journal of Nuclear Medicine, vol. 50, no. 1, p. 139, 2009. [PubMed: 19139188]

[30]. Wang Y, Seidel J, Tsui BM, Vaquero JJ, and Pomper MG, "Performance evaluation of the GE healthcare explore VISTA dual-ring small-animal PET scanner," 2006.

[31]. España S, Marcinkowski R, Keereman V, Vandenberghe S, and Van Holen R, "DigiPET: sub-millimeter spatial resolution small-animal PET imaging using thin monolithic scintillators," Physics in Medicine & Biology, vol. 59, no. 13, p. 3405, 2014. [PubMed: 24888974]

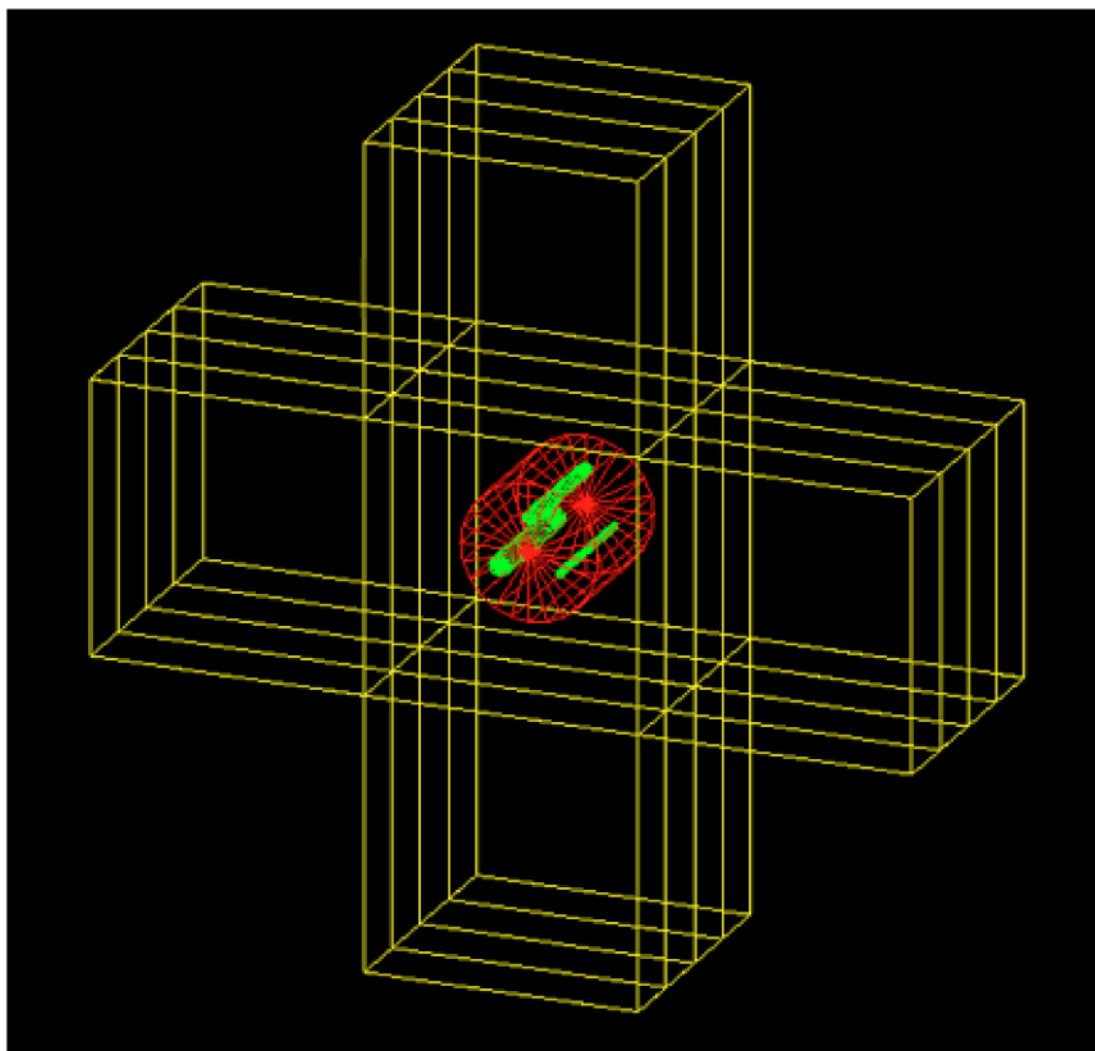**Fig. 1.**
The CZT system (yellow), contrast phantom (red), and compartments (green) were modeled in GATE. The diameters of the compartments were 1, 2, and 3 mm respectively.
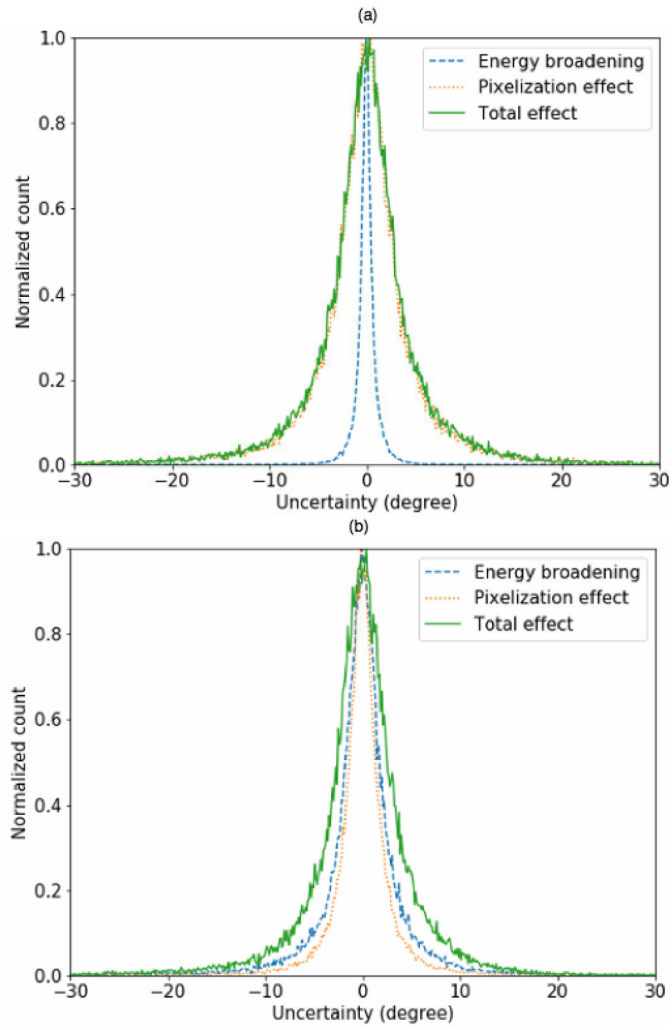
Fig. 2.
Uncertainty distribution with (a) 1% energy resolution and $1 \times 1 \times 1$ mm^3 spatial resolution (b) 4% energy resolution and $0.5 \times 0.5 \times 0.5$ mm^3 spatial resolution. Total effect includes the energy broadening and pixelization effect.
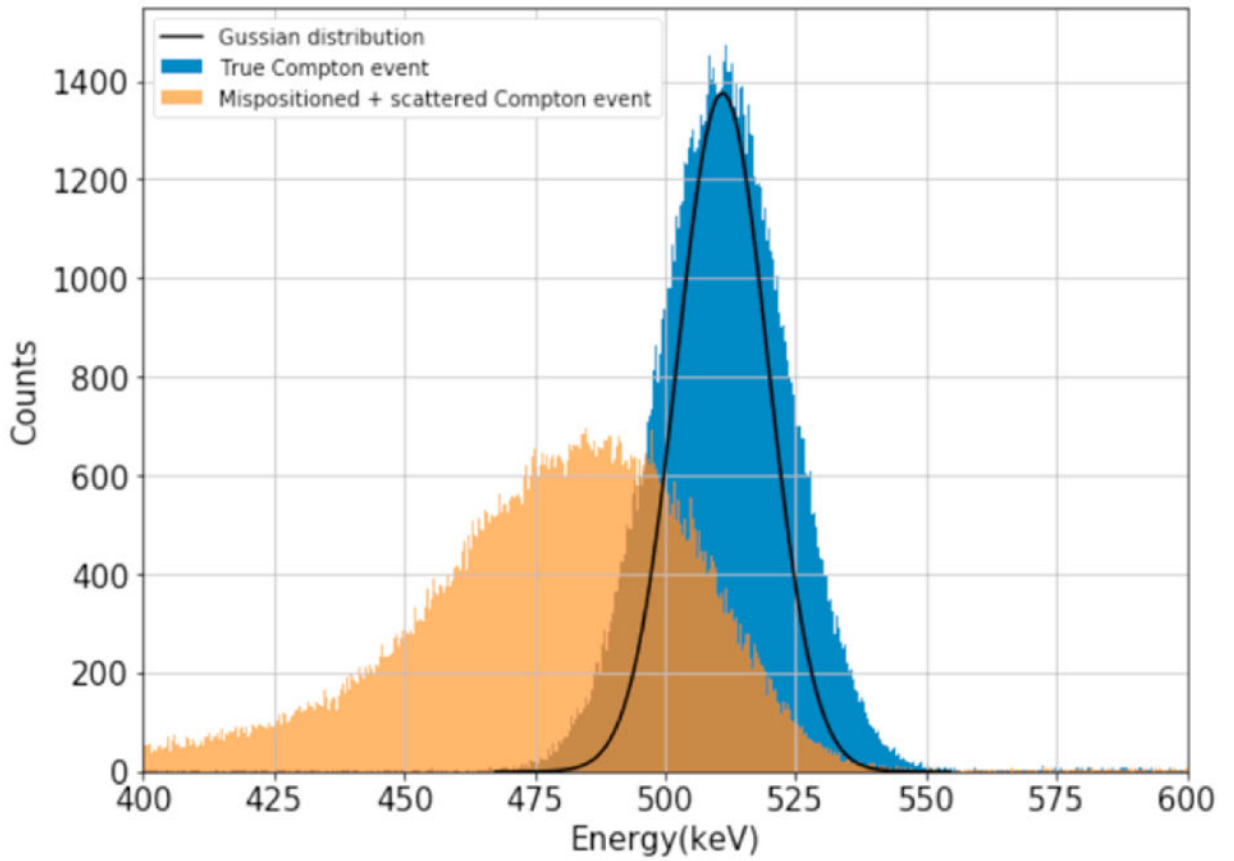
Fig. 3.
Compton energy spectrum with the electronic noise limited blurring method. The energy resolution was 4% FWHM at 511 keV. Blue represents the true Compton events, orange represents mispositioned and scattered Compton events. The solid black line is an ideal Gaussian distribution with a FWHM of 20.44 keV.

Fig. 4.
Compton energy spectrum with the statistic noise limited blurring method. The energy resolution was 4% FWHM at 511 keV. Blue represents the true Compton events, orange represents mispositioned and scattered Compton events. The solid black line is an ideal Gaussian distribution with a FWHM of 20.44 keV.
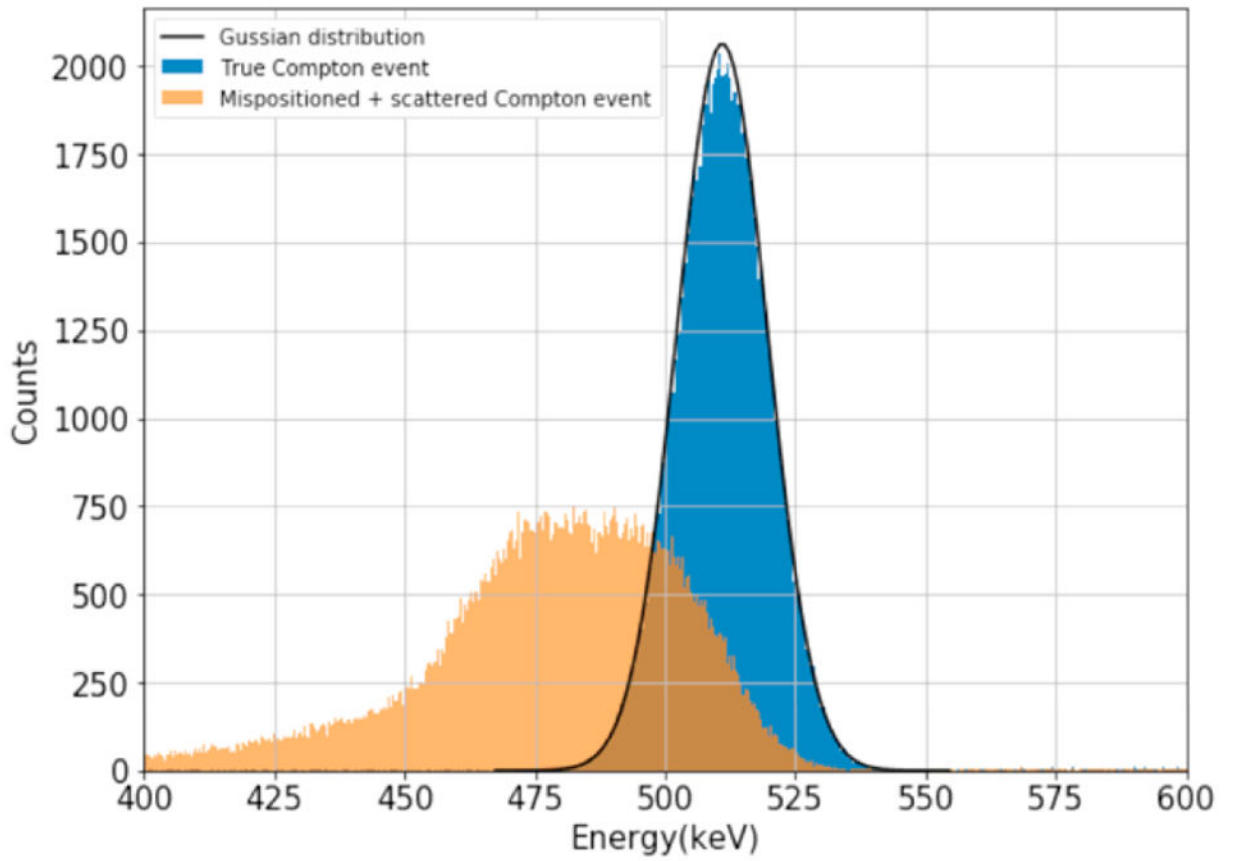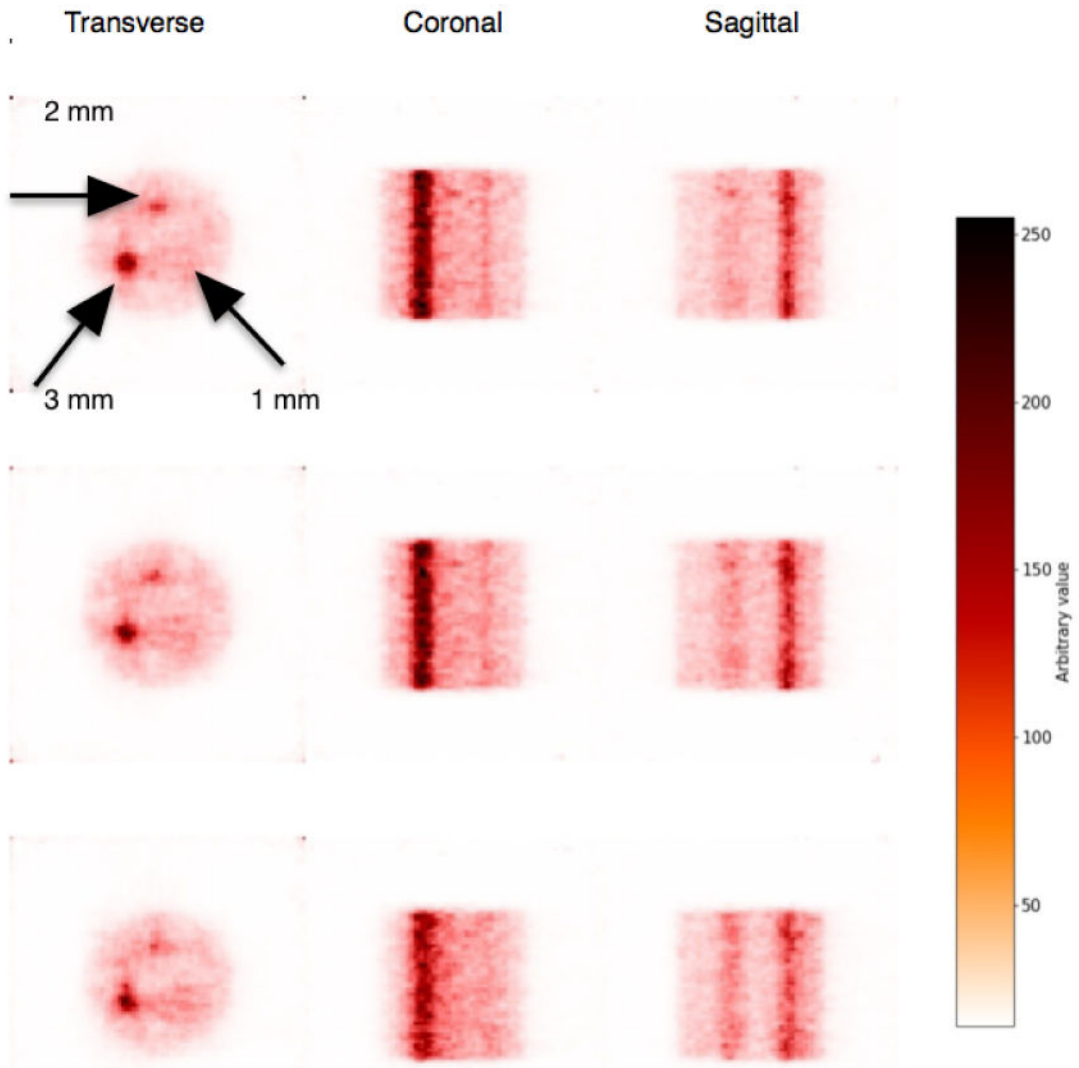
Fig. 5.
Transverse, coronal, and sagittal views of the reconstructed images of PP coincidences with normalization. The first row is 1% energy and $0.5 \times 0.5 \times 0.5$ mm^3 spatial resolution. The second row is 1% energy and $1 \times 1 \times 1$ mm^3 spatial resolution. The third row is 4% energy and $1 \times 3 \times 0.5$ mm^3 spatial resolution.
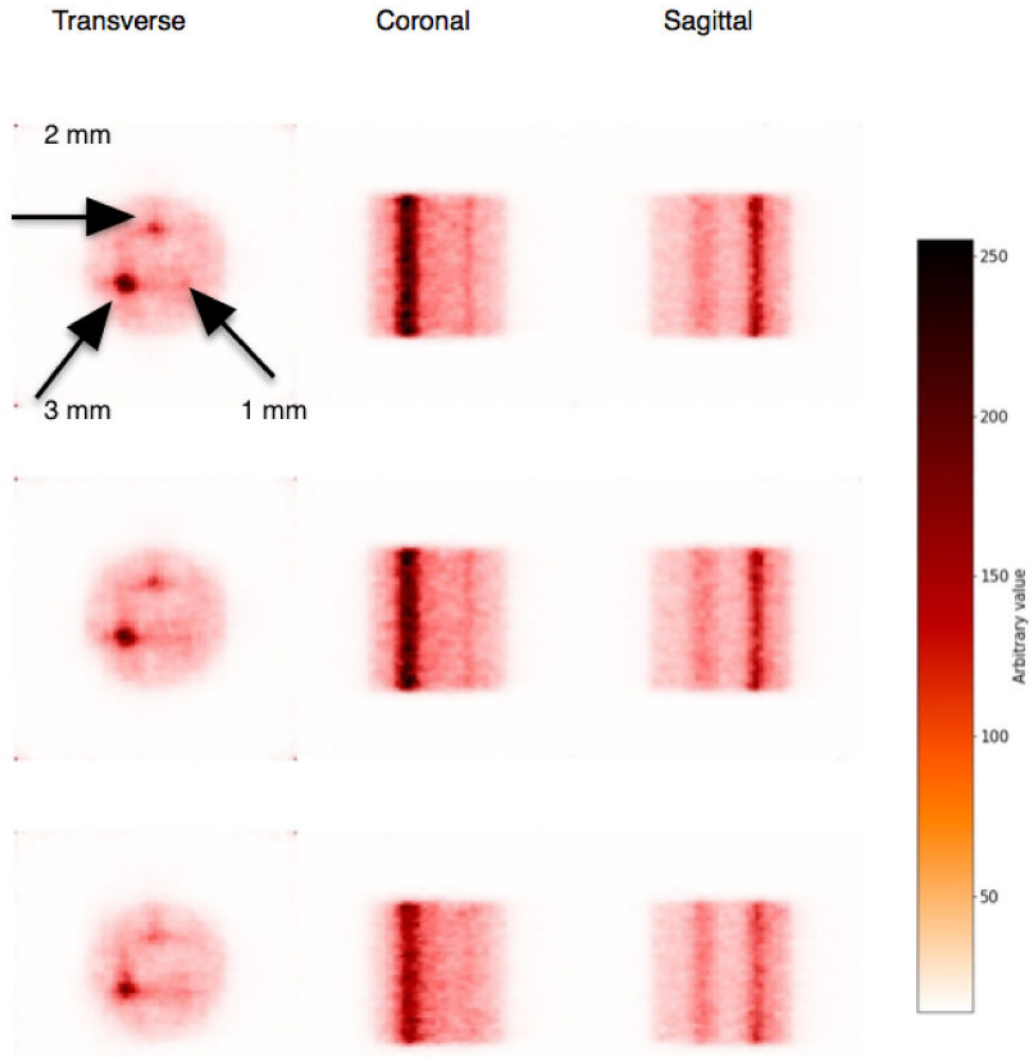
Fig. 6.
Transverse, coronal, and sagittal views of the reconstructed images of PP and PC coincidences with normalization. The first row is 1% energy and $0.5 \times 0.5 \times 0.5$ mm^3 spatial resolution. The second row is 1% energy and $1 \times 1 \times 1$ mm^3 spatial resolution. The third row is 4% energy and $1 \times 3 \times 0.5$ mm^3 spatial resolution.
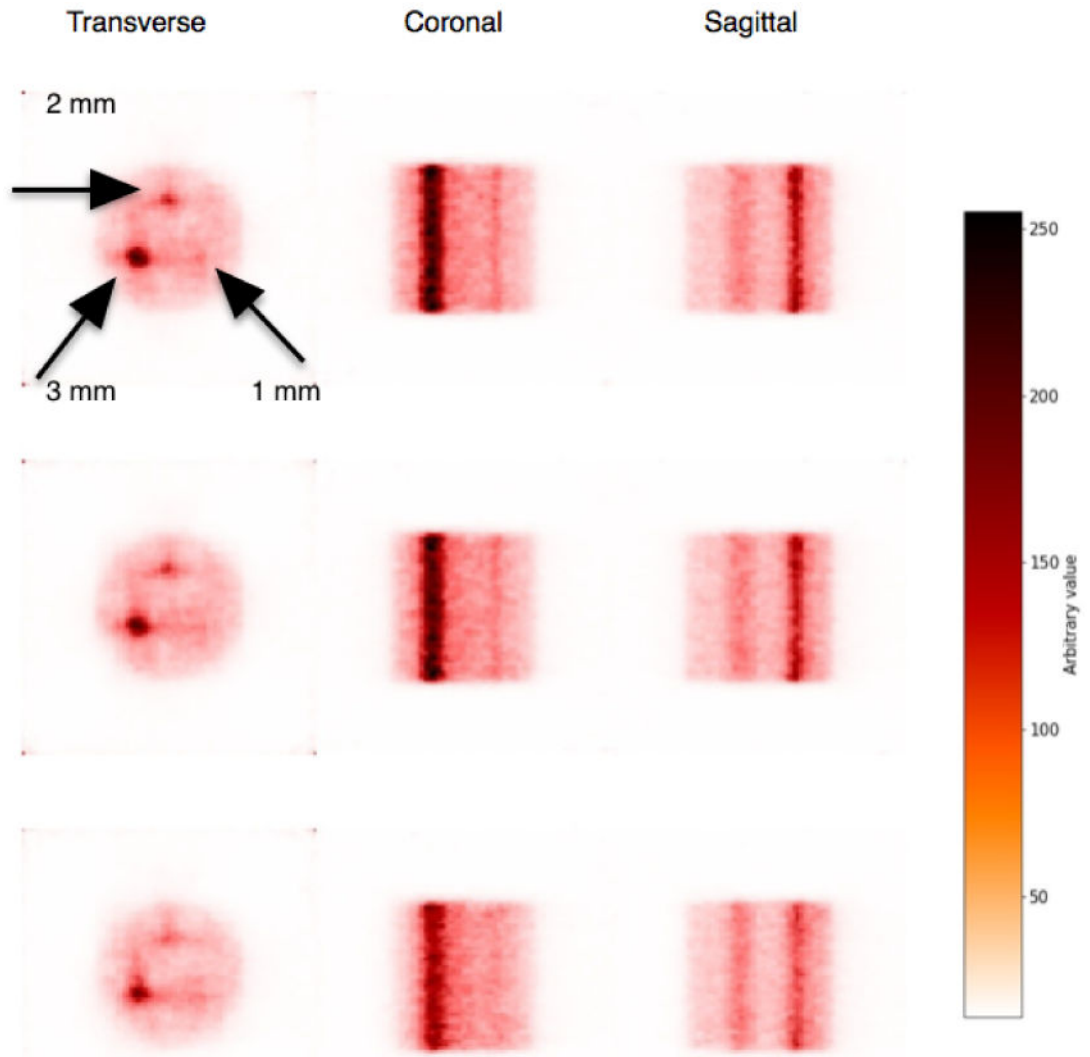
Fig. 7.
Transverse, coronal, and sagittal views of the reconstructed images of randomly-selected coincidences with normalization. The first row is 1% energy and $0.5 \times 0.5 \times 0.5$ mm^3 spatial resolution. The second row is 1% energy and $1 \times 1 \times 1$ mm^3 spatial resolution. The third row is 4% energy and $1 \times 3 \times 0.5$ mm^3 spatial resolution.

TABLE I

Distribution (in percentage) of single 511 keV events recorded in a CZT system with different energy thresholds, where Co = Compton, Pe = photoelectric. Energy threshold was applied to the same simulation data after energy blurring in post processing and events below the energy threshold were dropped. The base for calculating the percentage for different thresholds was the total number of 511 keV events when the threshold was set to 10 keV.

Ethreshold (keV)	Pe only	1Co 1Pe	2Co 1Pe	3Co 1Pe	>4Co 1Pe
10	24.4	37.6	24.4	9.9	3.7
50	26.4	43.4	20.2	3.6	0.29
100	26.4	40.3	8.9	0.19	0

TABLE II

The average error($\bar{\sigma}_{\theta_E}$, $\bar{\sigma}_{\theta_P}$, $\bar{\sigma}_{\theta_{DDA}}$) of θ_E, θ_P, and θ_{DDA} of PC coincidences with energy resolution of 1%, 4% and 6% and different spatial resolutions.

Energy resolution (%)	Spatial resolution (x×y×z) mm³	$\bar{\sigma}_{\theta_E}$ (°)	$\bar{\sigma}_{\theta_P}$ (°)	$\bar{\sigma}_{\theta_{DDA}}$ (°)
1	$0.5 \times 0.5 \times 0.5$	0.67	1.94	2.17
1	$1 \times 1 \times 1$	0.67	3.75	3.89
4	$1 \times 3 \times 0.5$	2.65	9.24	10
4	$1 \times 3 \times 1$	2.65	9.30	10
4	$1 \times 5 \times 1$	2.65	13.43	13.91
6	$1 \times 5 \times 1$	3.97	13.43	14.41

TABLE III

The percentage decrease of PC coincidences with 482 and 493 keV lower energy bounds while the upper bound was fixed at 551 keV. The energy blurring method was electronic noise limited. All the values in columns were compared with the values of 471 keV lower bound case.

Lower bound (keV)	T(%)	C(%)	S(%)	R(%)
482 (−1.5 FWHM)	1	27	25	3
493 (−1 FWHM)	13	57	54	15

TABLE IV

The percentage decrease of PC coincidences with 482 and 493 keV lower energy bounds while the upper bound was fixed at 551 keV. The energy blurring method was statistic noise limited. All the values in columns were compared with the values of 471 keV lower bound case.

Lower bound (keV)	T(%)	C(%)	S(%)	R(%)
482 (−1.5 FWHM)	0.16	29	25	1.3
493 (−1 FWHM)	6	59	52	9

TABLE V

The percentage of true coincidences over the sum of true and mispositioned coincidences for photoelectric-photoelectric coincidences (PP) and photoelectric-Compton coincidences (PC). A system with 4% energy resolution at 511 keV, a 493–551 keV energy window, and $1 \times 3 \times 0.5$ mm^3 spatial resolution was considered.

Threshold (keV)	PP (%)	PC (%)
0	100	100
50	92.7	84.2

TABLE VI

The percentage of PC coincidences that were accurately recovered by Compton recovery algorithm.

Energy resolution (%)	Spatial resolution (mm^3)	Accurately recovered (%)
1	$0.5 \times 0.5 \times 0.5$	79.1
1	$1 \times 1 \times 1$	78.4
4	$1 \times 3 \times 0.5$	66.6

TABLE VII

The sensitivity of different systems with and without Compton recovery.

Energy resolution (%)	Spatial resolution (mm³)	Without Compton recovery (%)	With Compton recovery (%)
1	$0.5 \times 0.5 \times 0.5$	0.72	3.05
1	$1 \times 1 \times 1$	0.72	3.04
4	$1 \times 3 \times 0.5$	0.70	2.70

TABLE VIII

Geometric parameters of scintillator-based small-animal PET systems.

System name	Crystal element size(mm^3)	No. of crystal ring	Material	Axial length (mm)	Crystal ring diameter(mm)	Estimated solid angle* (sr)	Sensitivity (%)
Inveon [31]	$1.5 \times 1.5 \times 10$	80	LSO	127	161	6.03	7
VISTA [30]	$1.45 \times 1.45 \times (8+7)$	26	LYSO/GSO	48	118	4.27	4
CZT system	FOV (x×y×z mm^3) $40 \times 40 \times 40$					-	-
						7.91	3

*The solid angle was calculated by the system surface area of detectors divided by a spherical surface. The radius of the spherical surface was the largest distance from the center to the system surface.

TABLE IX

CNR of reconstructed images with 1% and 4% resolution and different spatial resolution.

Energy resolution (%)	1		1		4	
Spatial resolution (x×y×z) mm³	0.5 × 0.5 × 0.5		1 × 1 × 1		1 × 3 × 0.5	
Coincidence type	PP	PP + PC	PP	PP + PC	PP	PP + PC
3 mm hot rod	23.12 ± 7.72	31.82 ± 8.22	21.63 ± 8.37	29.85 ± 10.42	19.12 ± 11.79	24.25 ± 8.8
2 mm hot rod	15.14 ± 5.45	23.08 ± 6.52	15.31 ± 6.03	22.17 ± 7.46	12.74 ± 7.78	14.56 ± 5.23
1 mm hot rod	4.37 ± 1.61	6.63 ± 2.38	3.81 ± 1.76	6.18 ± 2.36	3.83 ± 2.21	5.96 ± 2.06

TABLE X

Contrast of reconstructed images with 1% and 4% resolution and different spatial resolution.

Energy resolution (%)	1		1		4	
Spatial resolution (x×y×z) mm³	0.5 × 0.5 × 0.5		1 × 1 × 1		1 × 3 × 0.5	
Coincidence type	PP	PP + PC	PP	PP + PC	PP	PP + PC
3 mm hot rod	2.74 ± 0.1	2.91 ± 0.12	2.7 ± 0.18	2.77 ± 0.07	2.05 ± 0.07	2.25 ± 0.02
2 mm hot rod	2.33 ± 0.42	2.59 ± 0.34	2.31 ± 0.43	2.36 ± 0.41	1.7 ± 0.35	1.8 ± 0.45
1 mm hot rod	1.72 ± 0.92	1.95 ± 0.95	1.69 ± 0.93	1.76 ± 0.92	1.26 ± 0.69	1.38 ± 0.69

TABLE XI

Percentage increase of CNR of reconstructed images after including PC coincidences

Energy resolution (%)	1	1	4
Spatial resolution (x×y×z) mm³	$0.5 \times 0.5 \times 0.5$	$1 \times 1 \times 1$	$1 \times 3 \times 0.5$
1 mm hot rod	51	62	55
2 mm hot rod	52	44	14
3 mm hot rod	37	38	26